Automatic Design System with Generative Adversarial Network and Vision Transformer for Efficiency Optimization of Interior Permanent Magnet Synchronous Motor

Yuki Shimizu, *Member*, *IEEE*

***Abstract*—Interior permanent magnet synchronous motors are becoming increasingly popular as traction motors in environmentally friendly vehicles. These motors, which offer a wide range of design options, require time-consuming finite element analysis to verify their performance, thereby extending design times. To address this problem, we propose a deep learning model that can accurately predict the iron loss characteristics of different rotor topologies under various speed and current conditions, resulting in an automatic design system for the IPMSM rotor core. Using this system, the computation time for efficiency maps is reduced to less than 1/3000 of the time required for finite element analysis. The system also shows efficiency optimization results similar to the best results of previous research, while reducing the computational time for optimization by one or two orders of magnitude.**

***Index Terms*—Design optimization, generative adversarial network, iron loss, permanent magnet motors, vision transformer.**

I. Introduction

IN the current era, the increasing integration of electrical and mechanical elements in a wide range of goods, along with the development of sustainable energy sources such as wind power generation, is being promoted to achieve carbon neutrality. As a result, the demand for machines that efficiently convert electrical power into mechanical action has increased dramatically. In the automotive industry, for example, there has been a remarkable global increase in the number of electric transportation systems, including electric cars, plug-in hybrid vehicles, and fuel cell units, along with the emergence of internal permanent magnet synchronous motors (IPMSMs), which are replacing internal combustion engines as the primary drive system in these electrified modes of transportation. In anticipation of continued growth in motor use in the future, improving the efficiency of IPMSMs remains a critical challenge.

The design phase of today's IPMSMs is prolonged due to two critical factors. First, the widespread use of finite element analysis (FEA) to calculate the characteristics of IPMSMs. Second, the wide range of design alternatives in these motors, including parts such as permanent magnets (PMs) and flux barriers, forces the iterative evaluation of numerous configurations to achieve defined standards. These combined factors lead to longer development times in IPMSM design, with multiple structures subjected to FEA and development based largely on the trial-and-error approach taken by designers.

Many studies have been conducted to reduce the time required for the optimal design of advanced IPMSMs by implementing machine learning (ML) methods [1]–[16]. Although ML-focused research requires a certain amount of training time, the computation takes less than 1/1000th of the time compared to FEA upon model completion [14]. Previous studies can be divided into those that use geometric parameters as input and those that use topology information. The former method takes the dimensions and current conditions of the motor design as input and predicts the motor characteristics with high accuracy. The dimension of the input information is often fixed, and the applicable domain of the ML model is based on the initial geometry, making the method suitable after the conceptual design is completed. The latter approach interprets the material data under the polar coordinate of the rotor geometry for IPMSMs as tensors, allowing the use of deep learning (DL) image processing models such as convolutional neural networks (CNN) and vision transformers (ViT). Although this method is capable of handling multiple topologies, it results in an increase in training dataset size, model dimensions, and training time.

The above-mentioned studies encounter limitations in input features such as geometry type, current and speed conditions, and model output variables such as torque and efficiency, which hinder the construction of a comprehensive automatic design system for IPMSMs. Therefore, this study proposes a DL model capable of handling various input and output conditions, thus contributing to the development of an automatic design system for IPMSMs as shown in Fig. 1. The system uses a generative adversarial network (GAN), a type of deep generative model, to construct the rotor shape of IPMSMs, and promptly predicts the speed, torque, and iron loss characteristics using two different characteristic prediction models. Configured to include current and speed conditions in addition to rotor geometry data, these models enable fast, high-quality efficiency map generation during current vector control, such as maximum torque per ampere (MTPA) control and flux weakening (FW) control. This approach allows efficiency optimization for numerous rotor topologies at any speed and torque setting. The main contributions of this study are as follows:

a) The construction of a model that accurately predicts iron loss characteristics in IPMSMs with three different rotor topologies.
b) To propose a time-efficient automatic design system for motor efficiency at arbitrary speed and torque points.

This work was supported by JST, ACT-X Grant Number JPMJAX20AE, Japan.

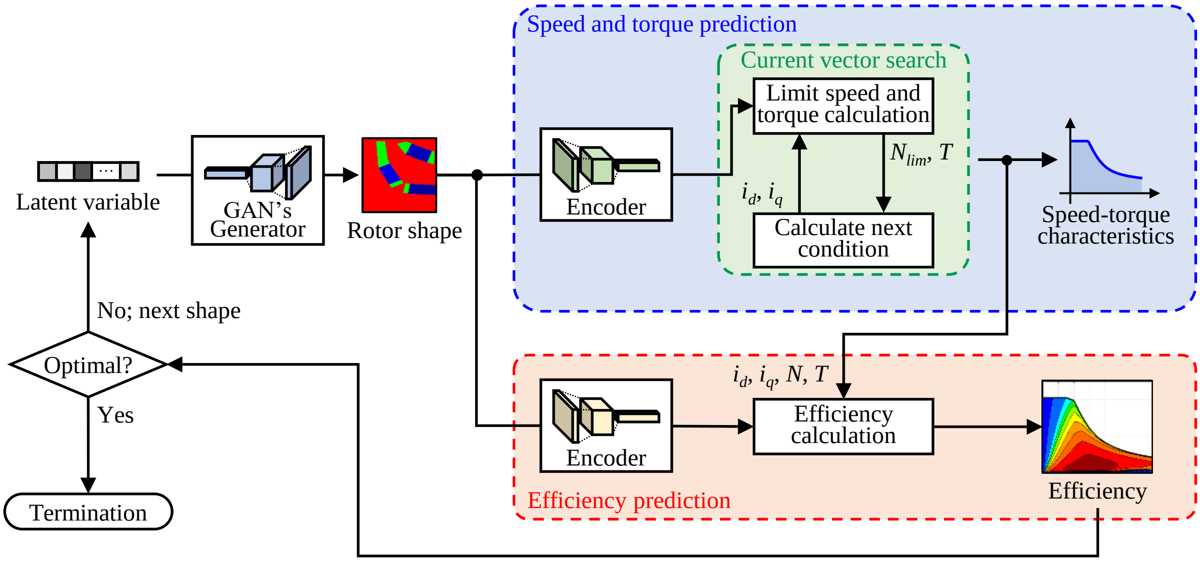

Fig. 1. Overall configuration of automatic design system for efficiency optimization. The blue part represents the prediction for the speed and torque characteristics using the model proposed in [16]. The red part represents the prediction for the iron loss characteristics, which is described in detail in Sec. III-C and IV.

c) To validate the reliability of the automatic design through FEA and prototype experimentation on the optimal geometry generated by the design system.

The dataset described in Sec. IV-A is available at IEEE DataPort [17]. This paper is an extended and revised version of a conference proceeding [18].

II. Related Works

A. Design Optimization without Machine Learning

Several studies have developed algorithms to efficiently determine the most appropriate design. Farhadian *et al.* [19] formulated an optimization mechanism, based on an improved particle swarm optimization, to enrich the torque aspects of a synchronous reluctance motor. Son *et al.* [20] improved the rotor arrangement of an IPMSM with grain-oriented electrical steel in the stator teeth, by applying a revised genetic algorithm. Das *et al.* [21] performed a sensitivity analysis on the noise vibration performance of the permanent magnet synchronous motor (PMSM) for 10 geometric parameters, and performed design optimization for the highly sensitive parameters. Pfister *et al.* [22] p proposed a method to perform an optimization of a PMSM assuming linear magnetic material properties, followed by FEA optimization with a small number of generations. Although these methods effectively optimize the geometry, they determine the motor characteristics only at a single or a small number of current settings, making them unsuitable for IPMSMs operating over wide current ranges, such as those used in automotive applications.

B. Shape Optimization with Machine Learning

To accelerate shape optimization, several research efforts have used machine learning to construct surrogate models as an efficient replacement for FEA. By using these surrogate models, we can perform the design of IPMSMs with a reduced reliance on FEA iterations, or potentially, without FEA at all. Islam *et al.* [1] used response surface methodology to optimize a pair of rotor design parameters at multiple output points of an IPMSM using the response surface methodology. Zheng *et al.* [2] performed multi-objective refinement of an IPMSM installed with rare earth PMs and ferrite PMs using the response surface methodology. Sun *et al.* [3] classified the geometric parameters of an IPMSM into three different groups using cross-factor variance analysis, and optimized them in terms of torque and loss characteristics by applying kriging. Sun *et al.* [4] proposed a sequential subspace optimization technique using the kriging method for a PM hub motor, respectively. Dhulipati *et al.* [5] used support vector regression to develop a predictive model for a six-phase IPMSM. Hao *et al.* [6] developed a model to identify the relationship between design parameters and torque ripple in an IPMSM using radial basis function networks, and used this model for optimization. Yan *et al.* [7] constructed a surrogate model using an artificial neural network for an IPMSM with a cage conductor embedded in the rotor and performed multi-objective optimization of torque, inertia, efficiency, power factor, and cogging torque. Zheng *et al.* [8] proposed an optimization method that combines ridge regression and the whale optimization algorithm for permanent magnet synchronous linear motors. Pan *et al.* [9] used XGBoost, a superior distributed gradient boosting library, to understand the relationship between the torque characteristics and the structural parameters of PM arc motors, and then used this model for optimization. Despite the demonstrated effectiveness of these machine learning-based surrogate models for automated IPMSM design, their ability to deal with geometric parameters within the same dimension is limited, restricting them to certain limited geometries.

C. Topology Optimization with Deep Learning

Various research efforts have introduced rotor design using topology optimization and DL. Barmada *et al.* [10] considered the incorporation of DL technology to optimize the rotor core topology of the synchronous reluctance motor (SynRM). Sasaki *et al.* [11] accelerated the rotor topology optimization of IPMSM with a CNN trained from the analysis of the magnetic flux distribution at the initial position and the material distribution. Sato *et al.* [12] predicted motor parameters from rotor geometry using CNNs and used the results to evaluate individuals in topology optimization. Khan *et al.* [13] optimized the topology of the SynRM rotor using deep reinforcement learning, a less biased approach to topology optimization compared to supervised learning. These research efforts are primarily focused on identifying innovative rotor designs and do not consider the wide operational range of properties and iron loss characteristics required for applications such as automotive settings.

III. Automatic Design System

A. Target Motor

This study focuses on IPMSMs for automotive applications. To verify the generality of the proposed method, this study uses three rotor topologies as shown in Fig. 2. All IPMSMs have 8-pole, 48-slot stators with distributed windings. Further specifications of each model can be found in [23].

B. Motor Design by Deep Generative Model

This study focuses on different rotor topologies and tries to handle them in a harmonious way by representing rotor geometries as images. Fig. 3 shows a schematic of the material representation approach implemented in the system. The rotor pole coordinates are specified as electrical steel sheets, PMs, or air. The image represents the rotor configuration by assigning one-hot vectors to the RGB pixels for each of the three materials, as shown in the right part of Fig. 3. A GAN generates the rotor image from a 256-dimensional latent variable space as follows.

$$\mathbf{x} = \mathcal{G}(\mathbf{z}), \tag{1}$$

where $\mathcal{G}$ is the generator of the GAN, $\mathbf{x}$ is the generated rotor image, $\mathbf{z}$ is the latent variable. See [16] for more details.

C. Prediction models

By predicting the characteristics from the generated images, an automatic design system can be constructed without FEA integration. This study uses geometry, current and speed conditions as input data, and considers models for predicting motor parameters and iron loss as follows.

$$\Psi_a, L_d, L_q = \mathcal{F}_1(\mathbf{x}, i_d, i_q), \tag{2}$$

$$W_h, W_e = \mathcal{F}_2(\mathbf{x}, i_d, i_q, N), \tag{3}$$

where $\mathcal{F}_1$ and $\mathcal{F}_2$ are the prediction models for motor parameters and iron loss, respctively, Ψ_a is the PM flux linkage, L_d and L_q are the d- and q-axis inductances, respectively, i_d and i_q are the d- and q-axis currents, respectively, N is the motor speed, and W_h and W_e are hysteresis loss and eddy current loss, respectively.

These models allow prediction of torque and efficiency aspects under various current vector control conditions as follows.

$$T = P_n \left\{ \Psi_a i_q + \left(L_d - L_q\right) i_d i_q \right\}, \tag{4}$$

$$\eta = \frac{\omega_m T - W_i}{\omega_m T + R_a I_a^2} = \frac{\omega_m T - \left(W_h + W_e\right)}{\omega_m T + R_a I_a^2}, \tag{5}$$

where P_n is the number of pole pairs, R_a is the winding resistance, I_a is the magnitude of the armature current vector, ω_m is the mechanical angular frequency, and W_i is the iron loss.

The model proposed in [16] is used for motor parameter prediction, and the iron loss prediction model is detailed in this section. Fig. 4 shows the common architecture of the iron loss prediction model used in this study, where d_{init} is the dimension of the encoded shape components, d_h and d_e are the dimensions of the hidden layers of the multilayer perceptron (MLP) for hysteresis loss and eddy current loss prediction, respectively, d_{ho} and d_{eo} are the dimensions of the second layer from the end of the MLP for hysteresis loss and eddy current loss prediction, respectively. FEA conditions, d- and q-axis currents and motor speed are standardized according to the following equations.

$$\bar{X} = \frac{X - \mu_X}{\sigma_X} \quad \left(X \in \left\{i_d, i_q, N\right\}\right), \tag{6}$$

where μ_X and σ_X are the mean and standard deviation of the training data, respectively.

As input, a trained model that encodes the rotor image generated by the GAN is used to extract the semantic rotor geometry data from the image. The resulting shape encoding information is combined with the FEA operating conditions in a multi-task learning context, allowing simultaneous prediction of hysteresis loss and eddy current loss. The MLP consists of fully connected layers and batch normalization, with a rectified linear unit (ReLU) serving as the activation.

$$Z^{(l+1)} = \phi\left(BN_{\gamma^{(l)},\beta^{(l)}}\left(W^{(l)} Z^{(l)} + B^{(l)}\right)\right), \tag{7}$$

$$BN_{\gamma^{(l)},\beta^{(l)}}\left(X^{(l)}\right) = \gamma^{(l)} \frac{X^{(l)} - \mathrm{E}\left[X^{(l)}\right]}{\sqrt{\mathrm{Var}\left[X^{(l)}\right] + \varepsilon}} + \beta^{(l)}, \tag{8}$$

$$\phi\left(X^{(l)}\right) = \mathrm{ReLU}\left(X^{(l)}\right) = \max\left(X^{(l)}, 0\right), \tag{9}$$

where $Z^{(l)}$ is the input to the l-layer, $W^{(l)}$ and $B^{(l)}$ are the weights and biases of the l-layer to be trained. In the batch normalization, the mean and standard deviation are computed per dimension over the mini-batches, $\gamma^{(l)}$ and $\beta^{(l)}$ are the learnable parameter vectors, and ε = 0.00001 is a constant added to the mini-batch variance for numerical stability.

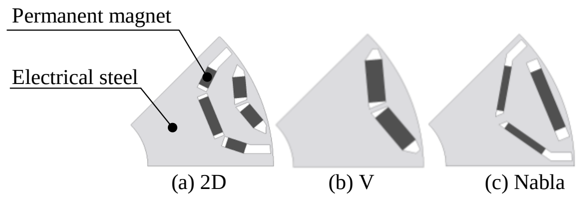

Fig. 2. Single-pole conventional rotor shapes.

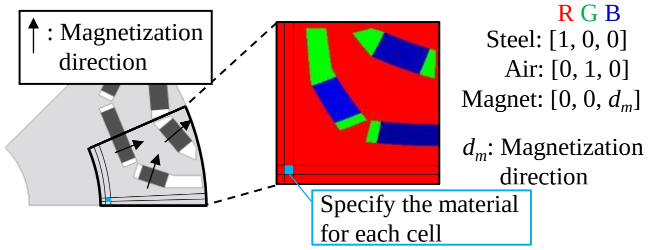

Fig. 3. Material representation of rotor shape.

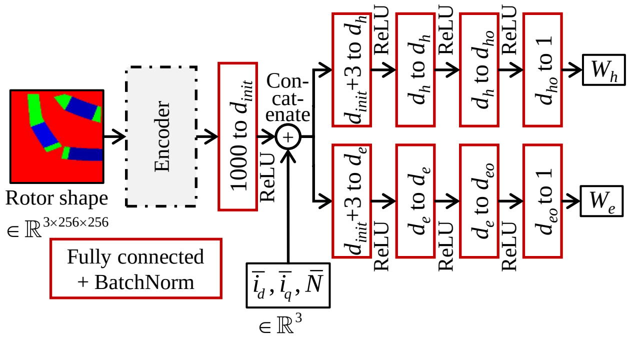

Fig. 4. Common architecture of iron loss prediction model.

IV. Training of Iron Loss Prediction Model

A. Dataset and Training Setting

To accommodate the large data requirements of deep learning, this study combines computer-aided design (CAD) and FEA for dataset generation. In terms of geometry, 30,000 shapes were formulated for each topology by randomly generating geometric parameters based on the three rotor topologies shown in Fig. 2. For these geometries, random FEA conditions, such as phase current (0–140 Arms), current phase (0–90°), and motor speed (0–15,000 r/min), were also generated, resulting in 90,000 FEA cases across the three rotor topologies. The motor characteristics to be calculated included core iron losses, specifically hysteresis and eddy current losses. The iron loss calculation was based on the fast Fourier transform (FFT) of the magnetic flux density and material data sheets. JMAG-Designer 19.1 software was used for analysis, yielding 85,184 datasets after excluding failed cases. See [15] for details.

80% of the dataset was used for training, while the remaining 20% was used for validation. The mean squared error (MSE) determined the loss function for multitask learning, as shown in the following equation.

$$\mathcal{L} = \mathcal{L}_h + \mathcal{L}_e = \frac{1}{n}\left(\sum_{i=1}^{n}\left(W_h^{(i)} - \hat{W}_h^{(i)}\right)^2 + \sum_{i=1}^{n}\left(W_e^{(i)} - \hat{W}_e^{(i)}\right)^2\right), \qquad (10)$$

where $W_h^{(i)}$ and $\hat{W}_h^{(i)}$ are the predicted hysteresis loss and training data, respectively, and $W_e^{(i)}$ and $\hat{W}_e^{(i)}$ are the predicted eddy current loss and training data, respectively.

The number of training epochs was set to 100. The optimizer was Adam, and the batch size was set to 128. PyTorch was used to implement the neural network model.

B. Hyperparameter Optimization

Hyperparameter optimization was performed on the iron loss prediction model shown in Fig. 4. The procedure started by using the tree-structured Parzen estimator (TPE) for hyperparameter optimization. Table I shows the variables to be optimized along with their upper and lower bounds, where n_l is the number of hidden layers in the MLP, lr is the learning rate of the optimizer. The Optuna library was used for the TPE [24]. During each optimization evaluation, a set of 20 epochs was assigned. The encoder model was the pre-trained Swin Transformer (Swin-T) [25], and the optimization results are shown in Table I.

Further comparative evaluations were performed based on the optimized hyperparameters of TPE. One focus was the comparison of hidden layer sizes in MLPs. Fig. 5 shows the validation loss differences for several d_h and d_e combinations, where the validation losses are evaluated at the end of the 100th training epoch and the listed validation losses are the mean values over 10 training runs. For d_h = 4, there is a significantly high validation loss for the hysteresis loss, which materializes independently of the d_e values, decreasing and reaching equilibrium as d_h increases. A parallel trend appears for the eddy current loss and d_e, indicating that an adequate representation of the nonlinearity within the iron loss characteristics occurs when the hidden layer dimensions exceed 10. In the following steps, (d_h, d_e) = (12, 10) is used because it produced the minimum validation losses for both hysteresis and eddy current losses.

Fig. 6 shows the validation loss for different n_l values to compare the influence of the number of the hidden layers in MLPs. The lowest validation loss for both hysteresis and eddy current loss is achieved with n_l = 3, and it increases as the number of layers increases beyond 3. This result suggests that it may not be necessary to rely on highly nonlinear models to predict iron loss from the encoded geometry data, motor speed, and current conditions. This is also supported by Steinmetz's experimental law [27], which states that the nonlinearity of hysteresis and eddy current loss is affected by up to a power of 1–2 with respect to the frequency (associated with speed) and the maximum flux density value (associated with current).

The evaluation of the shape encoder models is performed subsequently. Fig. 7 shows the validation loss associated with the weights of the Swin-T encoder weights, where "pre-trained" represents the encoder pre-trained using ImageNet [25], [28]–[31], and "normal" represents the model without pre-training. The contrast between "fix" and "train" refers to whether the encoder weights are fixed or additionally trained when training with the iron loss dataset. When comparing the validation loss, the observed minimum validation loss for both hysteresis loss and eddy current loss is achieved using a fixed weight encoder with pre-training.

TABLE I
Hyperparameters for Iron Loss Prediction Model

Symbols	Range	Selected by TPE
d_{init}	(2, 12)	8
d_h	(5, 55)	15
d_e	(5, 55)	10
d_{ho}	(10, 100)	50
d_{eo}	(10, 100)	50
n_l	(3, 11)	3
lr	(0.00001, 0.1)	0.0004

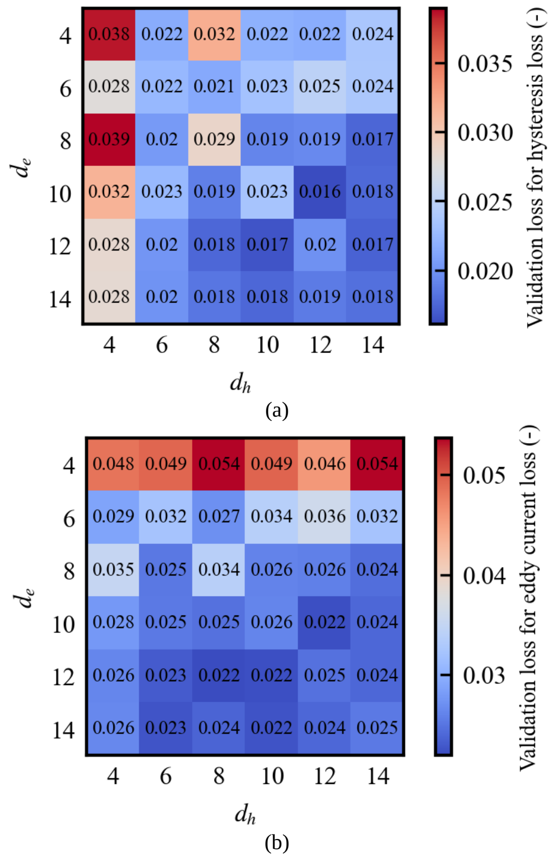

Fig. 5. Validation loss differences for several d_h and d_e combinations for (a) hysteresis loss and (b) eddy current loss. The mean values for 10 training runs are shown.

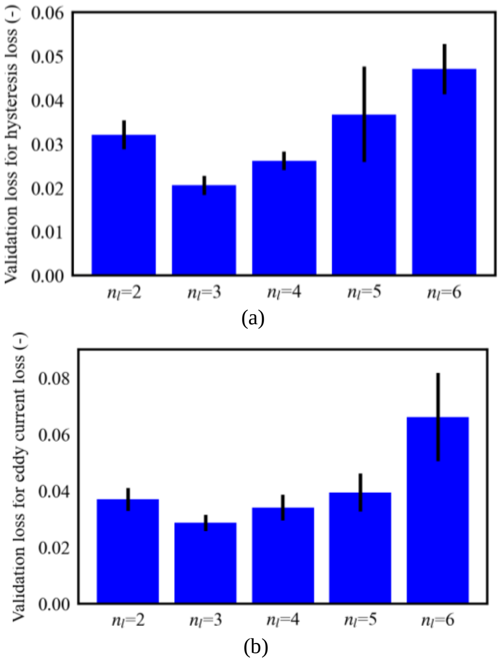

Fig. 6. Validation loss for different n_l for (a) hysteresis loss and (b) eddy current loss. The mean and standard deviation values for 10 training runs are shown.

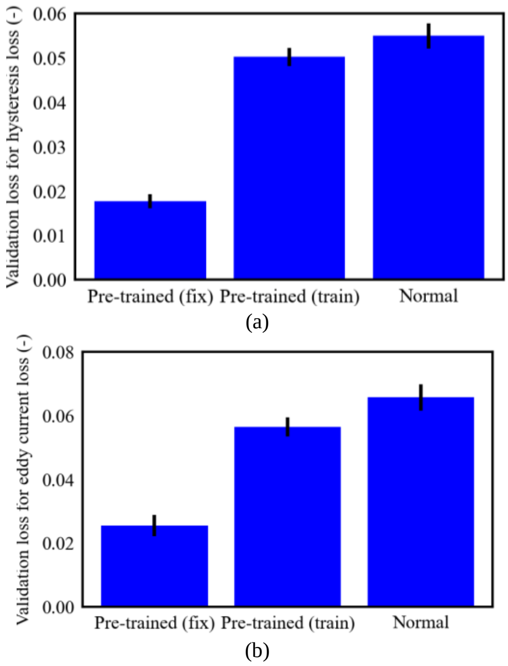

Fig. 7. Validation loss for different types of training for (a) hysteresis loss and (b) eddy current loss. The mean and standard deviation for 10 training runs are shown. "Pre-trained" represents the pre-trained encoder, and "normal" represents the model without pre-training. The contrast between "fix" and "train" refers to whether the encoder weights are fixed or additionally trained when training with the iron loss dataset.

Finally, the pre-trained models were compared. Table II shows the validation loss of several well-known encoder models [25], [28]–[31]. The final comparative evaluation shows that the Swin-T model produces the minimum validation loss, making it the most appropriate encoder model for this study.

V. Efficiency Optimization

The combination of the models described in Sec. IV results in the automatic design system for the IPMSM rotor core shown in Fig. 1. Using this design system, the efficiency optimization design is performed within the constraints of the

TABLE II

Validation Losses for Different Encoders

Model	Validation loss for W_h	Validation loss for W_e
ResNet-18 [28]	0.0539 ± 0.0117	0.0401 ± 0.0084
ResNet-34 [28]	0.0456 ± 0.0035	0.0369 ± 0.0114
ResNet-50 [28]	0.0562 ± 0.0145	0.0428 ± 0.0128
ResNet-101 [28]	0.0567 ± 0.0126	0.0447 ± 0.0050
ResNet-152 [28]	0.0570 ± 0.0050	0.0481 ± 0.0085
VGG-11 (w/bn) [29]	0.0289 ± 0.0025	0.0216 ± 0.0018
VGG-13 (w/bn) [29]	0.0267 ± 0.0018	0.0218 ± 0.0020
VGG-16 (w/bn) [29]	0.0357 ± 0.0089	0.0272 ± 0.0018
VGG-19 (w/bn) [29]	0.0310 ± 0.0034	0.0267 ± 0.0019
ViT-B/16 [30]	0.0429 ± 0.0051	0.0287 ± 0.0037
ViT-B/32 [30]	0.0348 ± 0.0064	0.0292 ± 0.0037
ViT-L/16 [30]	0.0346 ± 0.0042	0.0268 ± 0.0035
ViT-L/32 [30]	0.0378 ± 0.0053	0.0317 ± 0.0027
Swin-T [25]	**0.0267 ± 0.0033**	**0.0177 ± 0.0011**
Swin-B [25]	0.0406 ± 0.0092	0.0279 ± 0.0027
Poolformer-s12 [31]	0.0577 ± 0.0084	0.0428 ± 0.0104

*mean ± std for 10 training runs

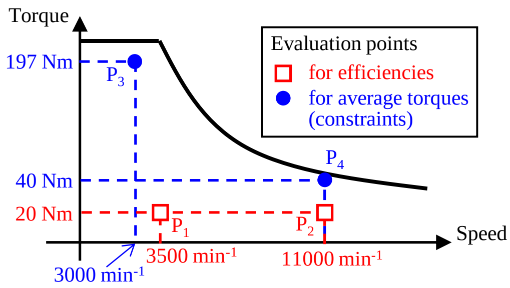

Fig. 8. Evaluation points used for optimization. The blue points are for efficiency evaluation. The red squares are for average torque constraints.

256-dimensional latent variable space found in the generative model.

A. Problem

In this study, the efficiency maximization design is performed at two unique evaluation points, constrained by two torque limits, as shown in Fig. 8. The efficiency maximization problem, incorporating a torque constraint for the IPMSM, is formulated as follows.

$$\min_{\mathbf{z}} \left(-\frac{\eta_1^{pred}}{\eta_1^{init}}, -\frac{\eta_2^{pred}}{\eta_2^{init}}\right)^T, \tag{11}$$

$$s.t.\quad g_i : T_i^{pred} \geq \alpha T_i^{req} \quad (i = 3, 4),$$

where η_1^{pred} and η_2^{pred} are the predicted efficiencies at operating points P_1 (3,000 r/min, 20 Nm) and P_2 (11,000 r/min, 20 Nm), with each value normalized by the initial values η_1^{init} and η_2^{init}, respectively. The constraint conditions g_i are the torque constraints for two required operating points P_3 (3,500 r/min, 197 Nm) and P_4 (11,000 r/min, 40 Nm), with a coefficient (α=1.05) to account for the prediction error.

Average torques, used in the efficiency evaluation and torque constraint analysis, were calculated using the motor parameter prediction model [16]. Current conditions for torque and efficiency calculations were determined by MTPA control and FW control algorithm [15].

NSGA-II [32] was used as the optimization algorithm, and the pymoo [33] library was used for implementation. The population size was 100, and the number of offspring was 10. Latin hypercube sampling was used for sampling the initial population, the tournament method was used for selection, simulated binary crossover was used for crossover, and polynomial mutation was used for mutation. The termination condition was set to 50 generations.

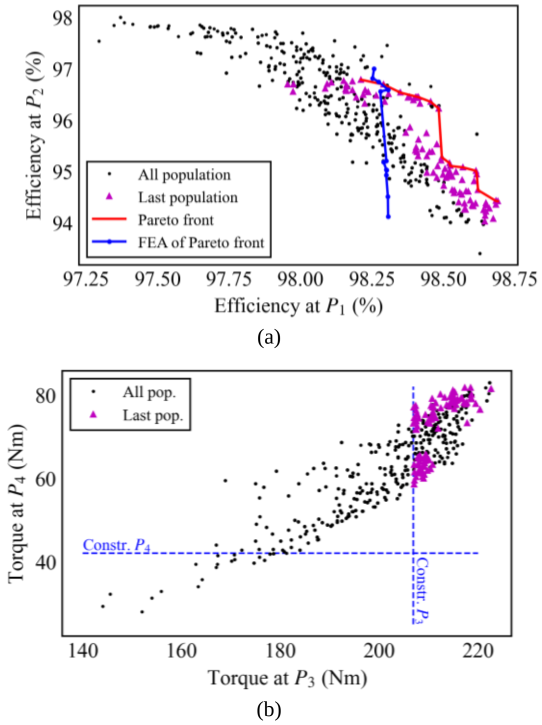

Fig. 9. Optimization result for (a) efficiencies and (b) torques using proposed automatic design system. The red line represents the Pareto front in the last generation. Individuals outside the Pareto front were eliminated in the optimization process because they did not satisfy the torque constraint. The blue line represents the result of the FEA performed on the individuals in the Pareto front.

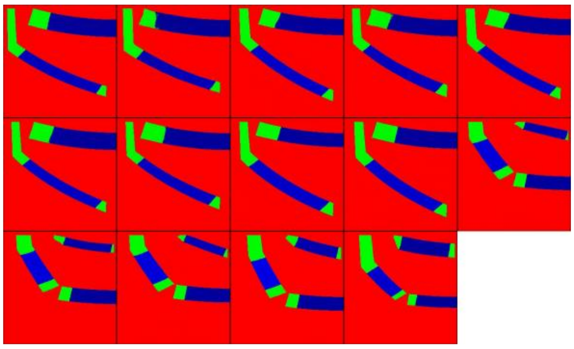

Fig. 10. Shapes of all Pareto solutions of optimization, which is indicated by the red line in Fig. 9(b).

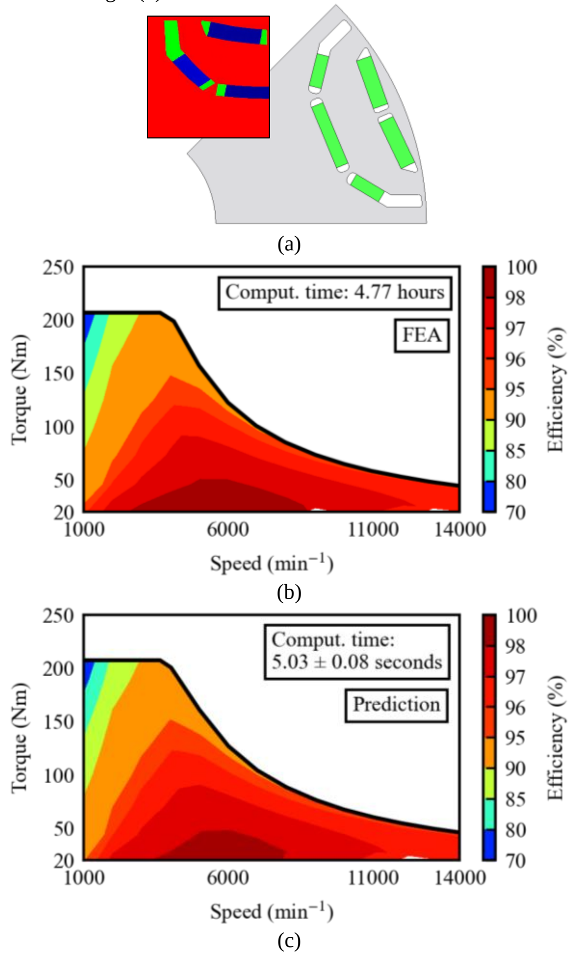

Fig. 11. Efficiency maps for selected optimal design. (a) Selected rotor geometry, and efficiency maps calculated by (b) FEA and (c) automatic design system.

B. Optimization Results

Fig. 9 shows the efficiency characteristics and torques at required speeds for all individuals in the optimization process, while Fig. 10 shows the Pareto solution shapes. After optimization, the final generation population established a clear Pareto front in terms of efficiencies. Notably, the entire final generation population satisfied the torque constraints, specifically the operating point constraint related to maximum torque was active. The final generation population is divided into two main clusters, representing Nabla and 2D topologies, as shown in Fig. 10. Nabla generally produces higher torque at low speed due to the proximity of the PMs to the gap, which reduces copper loss and increases efficiency at P_1. In contrast, the 2D topology is designed to mitigate gap flux density harmonics and preferentially achieves higher efficiency at high speeds P_2, where iron losses dominate.

Efficiency predictions for the Pareto front are usually better than those obtained from FEA, because tradeoff optimization with surrogate models tends to converge on individuals with overestimated solutions [14]. Nevertheless, the difference between the system predictions and the FEA results is marginal, highlighting the effectiveness of the system in predicting efficiencies with high accuracy. The efficiency prediction error at P_1 may appear large, but this is due to the more detailed scaling of the horizontal axis in Fig. 9(a) as opposed to the vertical axis, which actually results in a small prediction error.

To evaluate the efficiency characteristics in detail, the individual with the highest efficiency at P_2 was selected from among the Pareto solutions. Fig. 11 shows the selected rotor geometry, and the efficiency maps calculated by FEA and system prediction. The prediction accuracy of the efficiency characteristics is high, and the prediction system reduces the computational time required, with evaluations performed over 10 iterations using a computer with an Intel Core™ i7-9700K CPU, 32.0 GB of RAM, and an NVIDIA GeForce RTX 3090 SUPER (24 GB) GPU.

The optimization performance is further evaluated against previously proposed methods [15], namely parameter optimization with machine learning using XGBoost to predict torque and efficiency with geometric parameters of each topology. Table III shows a comparison of the losses of the optimized geometry under the Worldwide Harmonized Light Vehicles Test Cycle (WLTC) and the computational time for the optimization, where the WLTC losses were only evaluated during powering. The complete WLTC loss calculation procedure is described in [15]. An analysis of the results shows that the converging geometry of the proposed method has similar loss characteristics with the best result of previous parameter optimization approaches. Moreover, the

TABLE III
PERFORMANCE COMPARISON BETWEEN PROPOSED SYSTEM AND PARAMETER OPTIMIZATION

Item (unit)	Proposed	Parameter optimization (XGBoost) [15]		
		2D	V	Nabla
Loss under WLTC (FEA) (kJ)	**263.8**	**266.3**	329.7	311.7
− Copper loss (kJ)	199.1	206.1	232.0	229.3
− Iron loss (kJ)	64.7	60.2	97.7	82.4
Computation time for optimization (min)	**3.783 ± 0.037**	123.58 ± 0.13	55.25 ± 0.84	89.30 ± 0.23

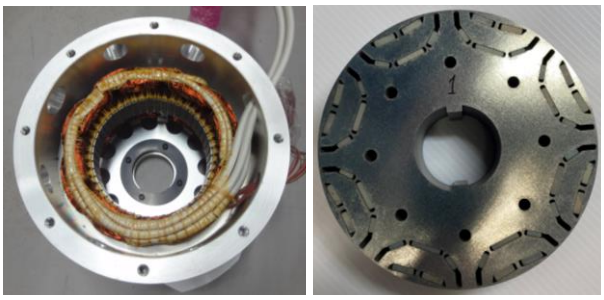

Fig. 12. Photographs of prototype. (a) Stator core. (b) Rotor core.

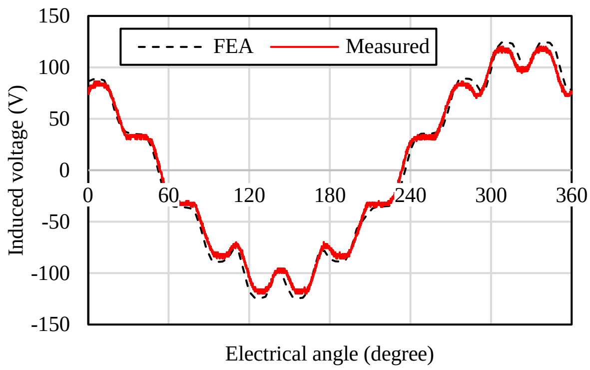

Fig. 13. Measured no-load induced voltage at 1200 r/min.

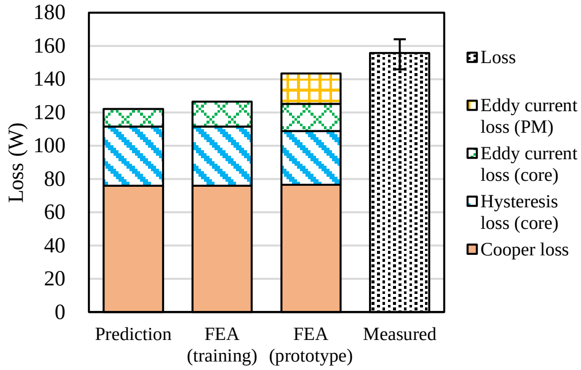

Fig. 14. Measured loss characteristics at 3500 r/min and 20 Nm.

computational time for optimization is reduced by one or two orders of magnitude due to the implementation of parallel processing on GPUs.

C.Experimental Validation

Finally, a prototype of the optimized geometry shown in Fig. 11(a) was fabricated for experimental validation of the proposed system. Fig. 12 shows the fabricated prototype rotor shape with minor adjustments to the PM positioning shape and the fillet pattern. In the experimental setup, the torque was measured by an SS-500 torque detector (Ono Sokki Co., Ltd., Yokohama, Japan), and the load was supplied by a 16-kW induction motor (Fuji Electronic Co., Ltd., Tokyo, Japan). A PWM inverter (Myway Plus Co., Yokohama, Japan) with a carrier frequency of 10 kHz and a DC side voltage of 650 V drove the tested IPMSMs.

Fig. 13 shows the no-load induced voltage, which is the line voltage between the U and V phases at 1200 r/min. The measured results are similar to the FEA results.

Fig. 14 shows the loss characteristics of the motor at a speed of 3500 r/min with a torque of 20 Nm, where the measured loss was calculated by subtracting the measured mechanical output and the electrical input to the motor, taking into account the pre-measured mechanical losses. "FEA (training)" represents an analysis result performed under conditions identical to the training dataset of the proposed system, while "FEA (prototype)" represents an analysis result performed under conditions adapted to the actual experiment. Specifically, the "FEA (prototype)" geometry adopts the same CAD data used in the prototype drawings, including PM positioning shape and fillets. In addition, it uses a finer analysis mesh and resolution, current input considerations for the PWM inverter, temperature condition, and eddy current loss analysis in the PM.

Direct comparisons between measured losses and system predictions indicate significant errors. On the other hand, comparing the system predictions with the FEA results under conditions equivalent to the training data shows a prediction error of 3.5%, indicating a high level of accuracy in the system prediction. This leads to the conclusion that the discrepancy between the measured losses and the system predictions is due to the modeling errors present in the FEA results of the training dataset. Furthermore, although the losses of "FEA (prototype)" were closer to the measured results than those of "FEA (training)", there are still differences between FEA and measured results due to factors such as three-dimensional iron losses, stray load losses, manufacturing tolerances, and variations in machine losses. In addition, the analysis time for "FEA (prototype)" exceeded that of "FEA (training)" by more than sixty times. Because a sufficient amount of data is required for deep learning models to cover a wide range of applications, the trade-off between modeling accuracy and FEA analysis time is the primary obstacle to improving the performance of deep learning in motor design.

VI. CONCLUSIONS

This study proposed a DL model that accurately predicts the iron loss characteristics in IPMSMs with three different rotor topologies under various speed and current conditions. In addition, the combination of this model and previously proposed models resulted in an automatic design system for the IPMSM rotor core. Using this system, the computation time for efficiency maps was less than 1/3000 that of FEA. In addition, the efficiency optimization results with this system showed the same level of performance as the best results of the previous studies, while the computation time for optimization is reduced by one or two orders of magnitude.

The experimental results of the optimized geometry showed that there was a significant error between the system predictions and the measured values in terms of motor losses.

This was caused by the modeling errors present in the FEA results of the training dataset rather than the accuracy of the DL model, suggesting that how to obtain a dataset with both sufficient quality and quantity is an important issue for improving the performance of deep learning in motor design.

ACKNOWLEDGMENT

We thank Prof. Shigeo Morimoto and Dr. Yukinori Inoue, Osaka Metropolitan University, for providing experimental facilities and for their cooperation in the prototyping.

REFERENCES

[1] M. S. Islam, M. Chowdhury, A. Shrestha, M. Islam, and I. Husain, “Multiload Point Optimization of Interior Permanent Magnet Synchronous Machines for High-Performance Variable-Speed Drives,” *IEEE Trans. Ind. Appl.*, vol. 57, no. 1, pp. 427–436, Jan. 2021.

[2] S. Zheng, X. Zhu, L. Xu, Z. Xiang, L. Quan, and B. Yu, “Multi-Objective Optimization Design of a Multi-Permanent-Magnet Motor Considering Magnet Characteristic Variation Effects,” *IEEE Trans. Ind. Electron.*, vol. 69, no. 4, pp. 3428–3438, Apr. 2022.

[3] X. Sun, Z. Shi, G. Lei, Y. Guo, and J. Zhu, “Multi-Objective Design Optimization of an IPMSM Based on Multilevel Strategy,” *IEEE Trans. Ind. Electron.*, vol. 68, no. 1, pp. 139–148, Jan. 2021.

[4] X. Sun, N. Xu, and M. Yao, “Sequential Subspace Optimization Design of a Dual Three-phase Permanent Magnet Synchronous Hub Motor Based on NSGA III,” *IEEE Transactions on Transportation Electrification*, pp. 1–1, 2022.

[5] H. Dhulipati, E. Ghosh, S. Mukundan, P. Korta, J. Tjong, and N. C. Kar, “Advanced Design Optimization Technique for Torque Profile Improvement in Six-Phase PMSM Using Supervised Machine Learning for Direct-Drive EV,” *IEEE Trans. Energy Convers.*, vol. 34, no. 4, pp. 2041–2051, Dec. 2019.

[6] J. Hao, S. Suo, Y. Yang, Y. Wang, W. Wang, and X. Chen, “Optimization of Torque Ripples in an Interior Permanent Magnet Synchronous Motor Based on the Orthogonal Experimental Method and MIGA and RBF Neural Networks,” *IEEE Access*, vol. 8. pp. 27202–27209, 2020.

[7] B. Yan, Y. Yang, and X. Wang, “Design of a Large Capacity Line-Start Permanent Magnet Synchronous Motor Equipped With Hybrid Salient Rotor,” *IEEE Trans. Ind. Electron.*, vol. 68, no. 8, pp. 6662–6671, Aug. 2021.

[8] Z. Zheng, J. Zhao, L. Wang, F. Dong, and X. Yang, “Efficient Optimization Design Method of PMSLM Based on Deep Adaptive Ridge Regression With Embedded Analytical Mapping Function,” *IEEE Trans. Ind. Electron.*, vol. 69, no. 8, pp. 8243–8254, Aug. 2022.

[9] Z. Pan and S. Fang, “Torque Performance Improvement of Permanent Magnet Arc Motor Based on Two-Step Strategy,” *IEEE Trans. Ind. Inf.*, vol. 17, no. 11, pp. 7523–7534, Nov. 2021.

[10] S. Barmada, N. Fontana, L. Sani, D. Thomopulos, and M. Tucci, “Deep Learning and Reduced Models for Fast Optimization in Electromagnetics,” *IEEE Trans. Magn.*, vol. 56, no. 3, #7513604, Mar. 2020.

[11] H. Sasaki, Y. Hidaka, and H. Igarashi, “Prediction of IPM Machine Torque Characteristics Using Deep Learning Based on Magnetic Field Distribution,” *IEEE Access*, vol. 10, pp. 60814–60822, 2022.

[12] H. Sato and H. Igarashi, “Deep learning-based surrogate model for fast multi-material topology optimization of IPM motor,” *COMPEL - The international journal for computation and mathematics in electrical and electronic engineering*, vol. 41, no. 3. pp. 900–914, 2022.

[13] A. Khan, C. Midha, and D. Lowther, “Reinforcement learning for topology optimization of a synchronous reluctance motor,” *IEEE Trans. Magn.*, vol. 58, no. 9, #8206204, Sep. 2022.

[14] Y. Shimizu, S. Morimoto, M. Sanada, and Y. Inoue, “Using Machine Learning to Reduce Design Time for Permanent Magnet Volume Minimization in IPMSMs for Automotive Applications,” *IEEJ J. Ind. Appl.*, vol. 10, no. 5, pp. 554–563, 2021.

[15] Y. Shimizu, “Efficiency Optimization Design That Considers Control of Interior Permanent Magnet Synchronous Motors Based on Machine Learning for Automotive Application,” *IEEE Access*, vol. 11, pp. 41–49, 2023.

[16] Y. Shimizu, S. Morimoto, M. Sanada, and Y. Inoue, “Automatic Design System With Generative Adversarial Network and Convolutional Neural Network for Optimization Design of Interior Permanent Magnet Synchronous Motor,” *IEEE Trans. Energy Convers.*, vol. 38, no. 1, pp. 724–734, Mar. 2023.

[17] Y. Shimizu, “Dataset for Iron Losses of IPMSMs.” IEEE Dataport, 19-Aug-2022.

[18] Y. Shimizu, “Investigation of Iron Loss Prediction Model for Automatic Design System of IPMSMs,” in *2023 24th International Conference on the Computation of Electromagnetic Fields (COMPUMAG)*, 2023.

[19] M. Farhadian, M. Moallem, and B. Fahimi, “Multimodal Optimization Algorithm for Torque Ripple Reduction in Synchronous Reluctance Motors,” *IEEE Access*, vol. 10, pp. 26628–26636, 2022.

[20] J.-C. Son, J.-Y. Kim, J.-W. Choi, D.-K. Lim, and H.-K. Yeo, “Performance Enhancement of the IPMSM for HEV Applications Using Grain-Oriented Electrical Steel and Design Optimization,” *IEEE Access*, vol. 10, pp. 46599–46607, 2022.

[21] S. Das *et al.*, “Sensitivity Analysis Based NVH Optimization in Permanent Magnet Synchronous Machines Using Lumped Unit Force Response,” *IEEE Transactions on Industry Applications*, vol. 58, no. 3. pp. 3533–3544, 2022.

[22] P.-D. Pfister, C. Tang, and Y. Fang, “A Multi-Objective Finite-Element Method Optimization That Reduces Computation Resources Through Subdomain Model Assistance, for Surface-Mounted Permanent-Magnet Machines Used in Motion Systems,” *IEEE Access*, vol. 11, pp. 8609–8621, 2023.

[23] Y. Shimizu, S. Morimoto, M. Sanada, and Y. Inoue, “Influence of Permanent Magnet Properties and Arrangement on Performance of IPMSMs for Automotive Applications,” *IEEJ J. Ind. Appl.*, vol. 6, no. 6, pp. 401–408, Nov. 2017.

[24] T. Akiba, S. Sano, T. Yanase, T. Ohta, and M. Koyama, “Optuna: A Next-generation Hyperparameter Optimization Framework,” in *Proceedings of the 25th ACM SIGKDD International Conference on Knowledge Discovery & Data Mining*, Anchorage, AK, USA, 2019, pp. 2623–2631.

[25] Liu *et al.*, “Swin Transformer: Hierarchical Vision Transformer using Shifted Windows,” in *2021 IEEE/CVF International Conference on Computer Vision (ICCV)*, 2021, vol. 0, pp. 9992–10002.

[26] C. P. Steinmetz, “On the law of hysteresis,” *Proc. IEEE Inst. Electr. Electron. Eng.*, vol. 72, no. 2, pp. 197–221, 1984.

[27] J. Deng, W. Dong, R. Socher, L.-J. Li, K. Li, and L. Fei-Fei, “ImageNet: A large-scale hierarchical image database,” in *2009 IEEE Conference on Computer Vision and Pattern Recognition*, 2009, pp. 248–255.

[28] K. He, X. Zhang, S. Ren, and J. Sun, “Deep Residual Learning for Image Recognition,” in *the International Conf. on Learning Representations (ICLR)*, 2016, pp. 770–778.

[29] K. Simonyan and A. Zisserman, “Very Deep Convolutional Networks for Large-Scale Image Recognition,” in *the International Conf. on Learning Representations (ICLR)*, 2015.

[30] A. Dosovitskiy *et al.*, “An Image is Worth 16x16 Words: Transformers for Image Recognition at Scale,” in *the International Conf. on Learning Representations (ICLR)*, 2021.

[31] W. Yu *et al.*, “Metaformer is actually what you need for vision,” in *Proceedings of the IEEE/CVF conference on computer vision and pattern recognition*, 2022, pp. 10819–10829.

[32] K. Deb, A. Pratap, S. Agarwal, and T. Meyarivan, “A fast and elitist multiobjective genetic algorithm: NSGA-II,” *IEEE Trans. Evol. Comput.*, vol. 6, no. 2, pp. 182–197, Apr. 2002.

[33] J. Blank and K. Deb, “Pymoo: Multi-Objective Optimization in Python,” *IEEE Access*, vol. 8, pp. 89497–89509, 2020.

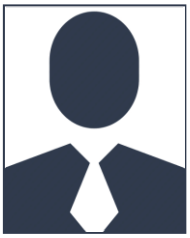

Yuki Shimizu (Member) received the B.E., M.E., and Ph.D. degrees from Osaka Prefecture University, Sakai, Japan, in 2016, 2018, and 2022, respectively. In 2018, he joined Toyota Motor Corporation, Aichi, Japan. In 2022, he joined the Graduate School of Science and Engineering, Ritsumeikan University, where he is currently an Assistant Professor. In 2023, he also founded MotorAI, Inc., where he is currently the Chief Executive Officer. His main research interests are the design and control of permanent magnet synchronous motors using machine learning and deep learning. Dr. Shimizu is a member of the Institute of Electrical Engineers of Japan, the Japan Institute of Power Electronics, and Society of Automotive Engineers of Japan.